Side-lobe level reduction in bio-inspired optical phased-array antennas

JULIÁN L. PITA,[1] **IVAN ALDAYA,**[2,3] **OCTÁVIO J. S. SANTANA,**[2]
LUÍS E. E. DE ARAUJO,[2] **PAULO DAINESE,**[2] **AND**
LUCAS H. GABRIELLI[1,*]

[1]*School of Electrical and Computer Engineering, University of Campinas (UNICAMP), 13083-852, Campinas, SP, Brazil*
[2]*Institute of Physics "Gleb Wataghin," University of Campinas (UNICAMP), 13083-859, Campinas, SP, Brazil*
[3]*Campus São João da Boa Vista, State University of São Paulo (UNESP), 13876-750, SP, Brazil*
[*]*lucashg@fee.unicamp.br*

Abstract: Phased arrays are expected to play a critical role in visible and infrared wireless systems. Their improved performance compared to single element antennas finds uses in communications, imaging, and sensing. However, fabrication of photonic antennas and their feeding network require long element separation, leading to the appearance of secondary radiation lobes and, consequently, crosstalk and interference. In this work, we experimentally show that by arranging the elements according to the Fermat's spiral, the side lobe level (SLL) can be reduced. This reduction is proved in a CMOS-compatible 8-element array, revealing a SLL decrement of 0.9 dB. Arrays with larger numbers of elements and inter-element spacing are demonstrated through a spatial light modulator (SLM) and an SLL drop of 6.9 dB is measured for a 64-element array. The reduced SLL, consequently, makes the proposed approach a promising candidate for applications in which antenna gain, power loss, or information security are key requirements.

References and links

1. P. Bharadwaj, B. Deutsch, and L. Novotny, "Optical antennas," Adv. Opt. Photonics **1**, 438–483 (2009).
2. M. F. Garcia-Parajo, "Optical antennas focus in on biology," Nat. Photonics **2**, 201–203 (2008).
3. A. Alù and N. Engheta, "Wireless at the nanoscale: optical interconnects using matched nanoantennas," Phys. Rev. Lett. **104**, 213902 (2010).
4. M. W. Knight, H. Sobhani, P. Nordlander, and N. J. Halas, "Photodetection with active optical antennas," Science **332**, 702–704 (2011).
5. D. Dregely, R. Taubert, J. Dorfmüller, R. Vogelgesang, K. Kern, and H. Giessen, "3D optical Yagi-Uda nanoantenna array," Nat. Commun. **2**, 267 (2011).
6. C. V. Poulton, M. J. Byrd, M. Raval, Z. Su, N. Li, E. Timurdogan, D. Coolbaugh, D. Vermeulen, and M. R. Watts, "Large-scale silicon nitride nanophotonic phased arrays at infrared and visible wavelengths," Opt. Lett. **42**, 21–24 (2017).
7. T. Komljenovic, R. Helkey, L. Coldren, and J. E. Bowers, "Sparse aperiodic arrays for optical beam forming and lidar," Opt. Express **25**, 2511–2528 (2017).
8. M. J. R. Heck, "Highly integrated optical phased arrays: photonic integrated circuits for optical beam shaping and beam steering," Nanophotonics **6**, 93–107 (2017).
9. K. V. Acoleyen, W. Bogaerts, J. Jágerská, N. L. Thomas, R. Houdré, and R. Baets, "Off-chip beam steering with a one-dimensional optical phased array on silicon-on-insulator," Opt. Lett. **34**, 1477–1479 (2009).
10. J. K. Doylend, M. J. R. Heck, J. I. Bovington, J. D. Peters, L. A. Coldren, and J. E. Bowers, "Two-dimensional free-space beam steering with an optical phased array on silicon-on-insulator," Opt. Express **19**, 21595–21604 (2011).
11. D. Kwong, A. Hosseini, J. Covey, Y. Zhang, X. Xu, H. Subbaraman, and R. T. Chen, "On-chip silicon optical phased array for two-dimensional beam steering," Opt. Lett. **39**, 941–944 (2014).
12. A. Yaacobi, J. Sun, M. Moresco, G. Leake, D. Coolbaugh, and M. R. Watts, "Integrated phased array for wide-angle beam steering," Opt. Lett. **39**, 4575–4578 (2014).
13. K. V. Acoleyen, H. Rogier, and R. Baets, "Two-dimensional optical phased array antenna on silicon-on-insulator," Opt. Express **18**, 13655–13660 (2010).

14. A. E. Krasnok, A. E. Miroshnichenko, P. A. Belov, and Y. S. Kivshar, "All-dielectric optical nanoantennas," Opt. Express **20**, 20599–20604 (2012).

15. H. Abediasl and H. Hashemi, "Monolithic optical phased-array transceiver in a standard SOI CMOS process," Opt. Express **23**, 6509–6519 (2015).

16. J. Sun, E. Timurdogan, A. Yaacobi, E. S. Hosseini, and M. R. Watts, "Large-scale nanophotonic phased array," Nature **493**, 195–199 (2013).

17. F. Aflatouni, B. Abiri, A. Rekhi, and A. Hajimiri, "Nanophotonic projection system," Opt. Express **23**, 21012–21022 (2015).

18. J. Kern, R. Kullock, J. Prangsma, M. Emmerling, M. Kamp, and B. Hecht, "Electrically driven optical antennas," Nat. Photonics **9**, 582–586 (2015).

19. A. Michaels and E. Yablonovitch, "Reinventing the circuit board with integrated optical interconnects," in "CLEO: Science and Innovations," (Optical Society of America, 2016), pp. STu4G–2.

20. C. A. Balanis, *Antenna Theory: Analysis and Design* (John Wiley & Sons, 2016).

21. R. J. Mailloux, *Phased Array Antenna Handbook*, vol. 2 (Artech House Boston, 2005).

22. J. Sun, E. S. Hosseini, A. Yaacobi, D. B. Cole, G. Leake, D. Coolbaugh, and M. R. Watts, "Two-dimensional apodized silicon photonic phased arrays," Opt. Lett. **39**, 367–370 (2014).

23. M. G. Bray, D. H. Werner, D. W. Boeringer, and D. W. Machuga, "Optimization of thinned aperiodic linear phased arrays using genetic algorithms to reduce grating lobes during scanning," IEEE T. Antenn. Propag. **50**, 1732–1742 (2002).

24. J. S. Petko and D. H. Werner, "The evolution of optimal linear polyfractal arrays using genetic algorithms," IEEE T. Antenn. Propag. **53**, 3604–3615 (2005).

25. M. A. Panduro, A. L. Mendez, R. Dominguez, and G. Romero, "Design of non-uniform circular antenna arrays for side lobe reduction using the method of genetic algorithms," AEU-INT J. Electron. C. **60**, 713–717 (2006).

26. M. M. Khodier and C. G. Christodoulou, "Linear array geometry synthesis with minimum sidelobe level and null control using particle swarm optimization," IEEE T. Antenn. Propag. **53**, 2674–2679 (2005).

27. S. K. Goudos, V. Moysiadou, T. Samaras, K. Siakavara, and J. N. Sahalos, "Application of a comprehensive learning particle swarm optimizer to unequally spaced linear array synthesis with sidelobe level suppression and null control," IEEE Antenn. Wirel. Pr. **9**, 125–129 (2010).

28. T. G. Spence and D. H. Werner, "Design of broadband planar arrays based on the optimization of aperiodic tilings," IEEE T. Antenn. Propag. **56**, 76–86 (2008).

29. M. D. Gregory, J. S. Petko, T. G. Spence, and D. H. Werner, "Nature-inspired design techniques for ultra-wideband aperiodic antenna arrays," IEEE Antenn. Propag. M. **52**, 28–45 (2010).

30. D. W. Boeringer, "Phased array including a logarithmic spiral lattice of uniformly spaced radiating and receiving elements," (2002). US Patent 6,433,754.

31. M. C. Viganó, G. Toso, G. Caille, C. Mangenot, and I. E. Lager, "Sunflower array antenna with adjustable density taper," Int. J. Antenn. Propag. **2009**, 1–10 (2009).

32. L. H. Gabrielli and H. E. Hernandez-Figueroa, "Aperiodic antenna array for secondary lobe suppression," IEEE Photonic Tech. L. **28**, 209–212 (2016).

33. J. N. Ridley, "Packing efficiency in sunflower heads," Math. Biosci. **58**, 129–139 (1982).

34. R. V. Jean, *Phyllotaxis: a Systemic Study in Plant Morphogenesis* (Cambridge University Press, 2009).

35. M. W. Niaz, Z. Ahmed, and M. B. Ihsan, "Reflectarray with logarithmic spiral lattice of elementary antennas on its aperture," AEU-Int. J. Electron.F C **70**, 1050–1054 (2016).

36. L. Dal Negro and S. Boriskina, "Deterministic aperiodic nanostructures for photonics and plasmonics applications," Laser & Photonics Reviews **6**, 178–218 (2012).

37. J. L. Pita, P. C. Dainese, H. E. Hernandez-Figueroa, and L. H. Gabrielli, "Ultra-compact broadband dielectric antenna," in "CLEO: Science and Innovations," (Optical Society of America, 2016), pp. SM3G–7.

38. J. A. Kurvits, M. Jiang, and R. Zia, "Comparative analysis of imaging configurations and objectives for Fourier microscopy," J. Opt. Soc. Am. A **32**, 2082–2092 (2015).

1. Introduction

Photonic antennas are used in a wide range of applications, including sensing, light detection and ranging (LIDAR), microscopy, wireless communications, photovoltaics, and holography [1–6]. To improve their radiation properties, power efficiency, and flexibility, significant effort has been dedicated to the development of optical antenna arrays in similar fashion to their radio-frequency counterparts [6–14]. Such approach enables a significant increase in overall directivity as well as dynamic control of the radiation pattern by tailoring both the amplitude and phase of each antenna element feeding [15–17]. This flexibility emerges as a significant feature in smart antennas required in future free-space communications [18]. In other applications, such as in multi-layer chip communication, however, static arrays are desirable in terms of cost and manufacturing

simplicity [19]. The arranging of several antennas is then employed mainly to enhance the radiation gain and increase the power transfer efficiency between layers. In these cases, complex integrated phase shifters and amplitude controllers can be avoided. The positions of the elements, however, become more critical.

In arrays of identical antennas, the far-field radiation pattern can be expressed as the product of the element radiation pattern and the array factor (AF), which depends on the excitation and position of each antenna element [20]. The AF can then be used to tailor the far-field radiation pattern without modifying the antenna element. For the sake of implementation simplicity and packing compactness, arrays with uniform element separation are often adopted [21]. Nevertheless, antenna arrays may present significant secondary lobes owing to the large separation between elements with respect to the wavelength, akin to grating lobes in a periodic grating. These secondary lobes are generally an undesired characteristic: they reduce the maximal power transmitted in the main lobe and they can lead to interference and security faults. A common metric to assess this feature is the side-lobe level (SLL), which is calculated as the ratio between the power of the strongest secondary lobe and the power of the main lobe. It is worth noting that, in the literature, the SLL has been used to characterize the total radiation pattern of arrays (which accounts for the radiation pattern of the antenna element) or only the AF. We adopted the latter approach, as we are interested mainly in the AF and not in the design of antenna element itself. In single element antennas, as well as in arrays where the element separation is smaller than half of the operation wavelength (λ), the secondary lobe has generally lower power than the main one and, therefore, the SLL is lower than 0 dB. However, in sparse antenna arrays, where the element separation exceeds $\lambda/2$, a periodic distribution of elements produces an AF having secondary lobes with the same power level as the main one, leading to a 0 dB SLL. This issue is critical in phased arrays operating in the infrared and visible wavelengths: the spatial resolution of state-of-the-art fabrication processes limits the minimal footprint of each antenna element as well as their separation. This separation grows even further, up to several λ-s, when the feeding network has to be implemented in the same layer.

Due to these extreme dimensions, reducing the SLL of optical phased array antennas is more challenging than in RF frequencies. Several approaches have been proposed to tackle this issue. For example, amplitude windowing (apodization) has shown to reduce the SLL in arrays for element separation lower than $\lambda/2$. Nonetheless, in sparse arrays, this approach does not reduce the power of grating lobes, leaving unaltered the array SLL [22]. In order to reduce the SLL of sparse antenna arrays, the position of elements has to be controlled. This has been performed in RF array antennas in several ways: genetic algorithms have been used in [23–25], whereas in [26, 27], particle swarm optimization has been employed. Optimization of aperiodic tilling has also been reported in [28, 29]. Apart from requiring long optimization processes, these solutions work in general only for large arrays with element separations not exceeding 5λ. Such scenario is typical in sparse RF antennas, but may not be suitable for photonic array antenna design.

A more promising approach has been adopted in [30–32] by employing a bio-inspired solution: the distribution of antenna elements according to Fermat's spiral, which is a particular case of an Archimedean spiral. This spiral appears in several biological systems, for instance in the morphogenesis of some cactus, the arrangement of seeds in sunflowers, and the shape of pine cones [33, 34]. This arrangement has been employed in RF and satellite communication applications with modest inter-element separation. Recently, Niaz and co-authors demonstrated the use of Fermat's spiral in a reflectarray at 16 GHz but with only 0.6λ linear spacing between elements [35].

Aperiodic structures in photonic devices have been studied by several groups—we highlight in particular the works by Dal Negro and Boriskina [36]—, but the SLL reduction in photonic antennas has not yet been experimentally demonstrated. In this paper, we show that arranging the antenna elements according to Fermat's spiral significantly reduces the SLL even in few-element

widely-spaced arrays, with a particular focus in integrated optics applications. Using conventional silicon platform for near-infrared, we show that regardless of the additional spacing required for the feeding network, an 8-element antenna array following the proposed design displays SLL approximately 1 dB lower than a periodic array of the same size. Additionally, by using an spatial light modulator (SLM) at visible wavelength (633 nm) to emulate larger arrays, we demonstrate that Fermat's spiral performs as expected for inter-element spacing of $581\,\lambda$ with up to 64 elements, a result far beyond what is usually considered as a sparse array. These results, reveal a 5.9 dB SLL suppression in a 25-element array and 6.9 dB in a 64-element array, following theoretical predictions.

2. Nanophotonic phased arrays

In order to design a low SLL antenna array operating at $\lambda = 1.55\,\mu m$, we employ the definition of the Fermat's spiral presented in [30–32] and implemented in [35]. According to the description of the spiral reported in the mentioned work, the position the n-th element of the array ($n = 1, 2, 3, \ldots, N$) in polar coordinates is given by:

$$\rho_n = \frac{d}{K}\sqrt{n} \tag{1}$$

$$\phi_n = n\pi\left(3 - \sqrt{5}\right) \tag{2}$$

where ρ_n is the distance of the n-th element to the origin, ϕ_n is its azimuthal angle, and $K = \sqrt{5 - 4\cos\phi_3} \approx 1.602$ is a normalization factor that ensures d to be the minimal separation between antennas (center-to-center). It is worth noting that the $n = 0$ element has been discarded because its distance to the first element is much smaller compared to the other distances between neighbors.

Because of maturity and reliability, the devices were fabricated at the imec/Europractice foundry, which implied several design constrains: on the one hand, they use 220 nm-high silicon-on-insulator (SOI) wafers with three different corrosion levels, resulting in four possible silicon heights: 0 (fully etched), 70, 150, and 220 nm (not etched). On the other hand, and more critically, fabrication resolution limited the minimum feature size in the mask as well as the minimum separation between elements. The fabricated arrays are formed of antenna elements similar to that presented in [37]. An important feature of this antenna design is the direction of maximum radiation, which is orthogonal to the substrate plane. This characteristic is critical in our measurements because it allows us to capture the main lobe of the element within the numerical aperture of the lens, thus leading to a better estimation of the AF. Figure 1 shows SEM images of the fabricated arrays with (a) uniform element distribution and (b) elements arranged according to Fermat's spiral. The fabricated antenna element [shown in the inset of Fig.1(b)] have a footprint of $1.78\,\mu m \times 1.78\,\mu m$, i.e., a square with sides of 1.15λ, posing an initial constrain on the element separation. The ultimate limit to this separation, however, arises from the feeding network, shown in Fig. 1(c), because of the required separation between the waveguides (1 µm) and the minimum bending radius (5 µm) to avoid cross-coupling and high losses.

Due to the complexity and size of the feeding network, we limit our analysis to 8 antenna elements. Nevertheless, this number could be significantly increased by further separating the antennas or by using a multi-layer feeding network. For comparison purposes, two different arrays were fabricated: a 4×2 array with a uniform element separation of 9 µm, and an array where the elements are arranged according to the Fermat's spiral with a minimum distance of $d = 9\,\mu m = 5.8\lambda$. The resulting footprints of the two fabricated arrays are similar, with the latter being only slightly larger. It is important to mention that in both arrays special care was taken to ensure that all elements were fed with the same signal power and phase. The power was equally divided among the 8 elements through a cascade of three stages of 3 dB splitters characterized at
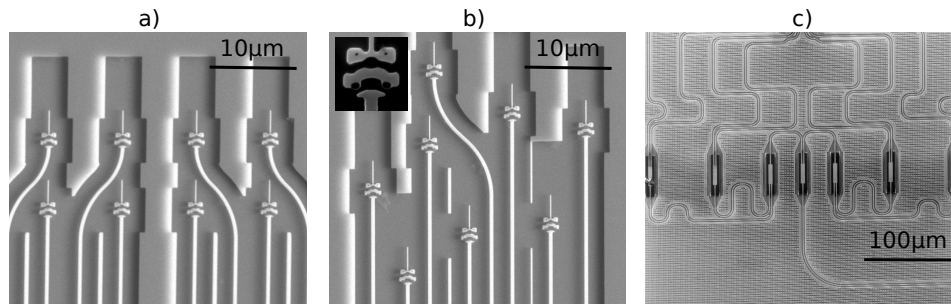
Fig. 1. SEM images of the fabricated SOI-based arrays and their feeding network. (a) uniformly distributed array antenna; (b) non-uniformly distributed array antenna; and (c) distribution network. The inset in (b) shows a zoom of the antenna element.

imec and showing an almost ideal 1:1 ratio. The phase in each antenna was designed to be the same by using waveguides with the same length, number of bends and bend radii for all elements, so that no tunning mechanism is necessary.

Figure 2(a) shows a picture of the setup used to characterize the fabricated antenna arrays together with the block diagrams for near-field [Fig. 2(b)] and far-field measurements [Fig. 2(c)]. Both measurements are proportional to the optical intensity but, while the former is related to the radiated field intensity on the surface of the elements (radiation sources), the latter corresponds to the radiated field in the Fraunhofer region (the term "near-field" is used here as is conventional in this area, since measurements reveal only the image of the radiating elements—reactive components of the near-field cannot be captured in this setup). A tunable laser source is set to emit at $\lambda = 1.55\,\mu\text{m}$. To optimize the polarization, the laser is followed by a polarization controller (PC), whose output is coupled into the SOI chip via a lensed fiber (LF) and an inverted taper fabricated on the chip. Two piezo-electric stages (PS) are employed to optimize and maintain the alignment. In order to measure the resulting near-field we built a $4f$-system composed of a 20× Mitutoyo Plan-Apo NIR infinity corrected objective L_1 (NA 0.4) and a second infinity corrected tube lens L_2 with a focal length of 200 mm, whereas to perform the measurement of the far-field radiation pattern, it is enough to simply remove L_2. It is worth noting that this single-lens arrangement may incur in image distortion when the effective area of the array antenna is large [38]. In our case, however, it shows good performance since the dimensions of the array are as small as $35\,\mu\text{m} \times 35\,\mu\text{m}$. In both near-field and far-field measurements, the images are captured employing a short wave infrared (SWIR) InGaAs CCD camera.
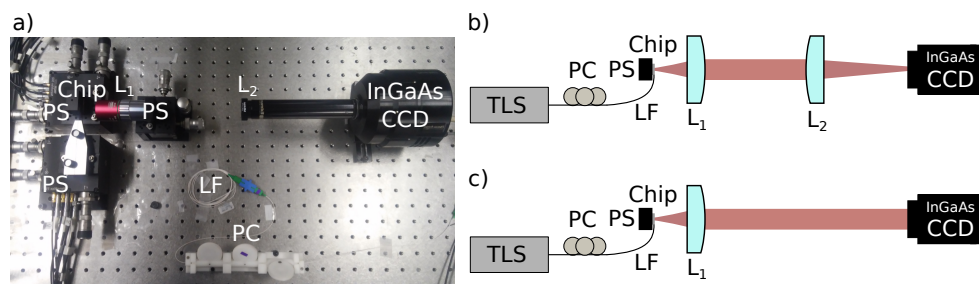

Fig. 2. Setup for near-field and far-field measurement of fabricated SOI-based array antennas at 1550 nm. (a) Photograph of the setup; (b) block diagram for near-field measurement; (c) block diagram for far-field measurement. PC: polarization controller, LF: lensed fiber, PS: piezo-electric stage, L_1: objective lens, and L_2: infra-red lens, and CCD: InGaAs camera.

We analyzed the SLL of the two fabricated SOI antenna arrays: the uniformly distributed array shown in Fig. 1(a) and the one with Fermat's spiral configuration, shown in Fig. 1(b). The position of the antenna elements can be clearly identified in the near-field measurement in both uniform [Fig. 3(a).i] and spiral [Fig. 3(a).ii] arrays, demonstrating that there is no radiation from the feeding network and that all antenna elements radiate with approximately the same intensity, as originally designed. Figure 3(b).i and (b).ii show the theoretical far-field patterns for both configurations. For each configuration, the far-field radiation patters was calculated by multiplying the radiation pattern of the antenna element (computed using finite difference in time domain method in Lumerical) and the theoretical far-field AF. The presence of high-intensity secondary lobes in the radiation pattern of the uniformly distributed array is clear in the form of multiple grating lobes of the array. For the spiral array, on the contrary, the main lobe dominates as the secondary lobes are spread out due to aperiodic antenna positioning. The SLL reduction is supported by the experimental measurements presented in Fig. 3(c).i and (c).ii for the uniform
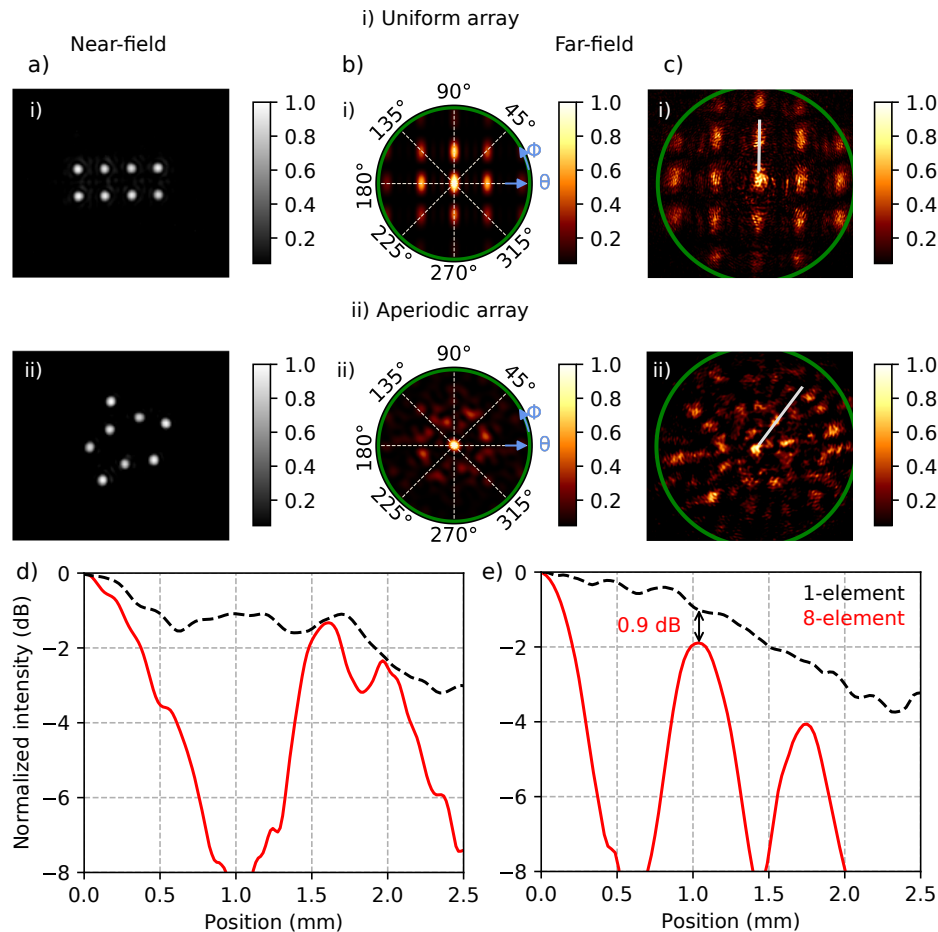

Fig. 3. Characterization of the fabricated photonic antennas: (i) uniformly distributed array and (ii) Fermat's spiral array. (a) near-field measurement, (b) simulated far-field radiation pattern, (c) measured far-field radiation pattern (the green circumference represents the numerical aperture of the objective, around 24°), (d) far-field radiation intensity for a single element and the uniformly distributed array in the azimuthal angle where the secondary lobe is more intense, and (f) same as (e) but for the spiral array.

and spiral arrays, respectively.

The side-lobes in the radiation pattern of the uniformly distributed array can be easily identified, having clean intensity valleys between them. This confirms that all the antenna elements are in-phase. In regards to the aperiodic array, we can see a single main lobe in the direction orthogonal to the substrate. The level of the side-lobe, however, can be appreciated more clearly when we plot the normalized intensity along a certain azimuthal angle. In our case, a fair comparison requires us to choose the angles at which the secondary lobe is more intense, which are identified in Fig. 3(c) as superimposed white lines. The resulting intensity levels for uniformly distributed and spiral arrays are presented in Fig. 3(e) and Fig. 3(f), respectively. Here, we performed 2D ideal interpolation to find intermediate points, which were subsequently filtered out using a 4th Savitzky–Golay filter to reduce the effect of the noise. Since we adopted the definition of SLL as the ratio between the side and main lobes of the AF, we first need to calculate the AF by computing the difference (in dB) between the normalized pattern of a single element and the normalized pattern of the array. Then, the SLL is found by looking for the maximum value of the AF apart from the main radiation lobe. Accordingly, we also plot the radiation pattern of a single element in the same azimuthal angle as reference and calculate the SLL as the difference between them. After performing this calculation, the results reveal that, as expected, the SLL of the uniformly distributed array is close to $0\,\mathrm{dB}$, whereas for the spiral array it is around $0.9\,\mathrm{dB}$. That is, we show a SLL reduction of almost 1 dB in the fabricated CMOS-compatible 8-element antenna array with a minimum element separation of 5.8λ.

3. Sparse arrays in visible range

The evaluation of the SLL reduction in arrays with higher number of elements was performed through emulation in the visible range of different array configurations using the setup shown in Fig. 4(a). As with the fabricated antenna, the far field measurements were performed using an optical $2f$-system. The element configuration, however, is not fixed, but can be modified by defining it on the SLM located at the Fourier plane of lens L_5. In this flexible setup, an optical beam from a continuous wave He-Ne laser operating at 633 nm is first coupled into a single-mode fiber to improve the purity of its fundamental mode. Afterwards, a 1 mm collimator (CO), a linear polarizer (LP), and a half-wave plate ($\lambda/2$) are used to adjust the beam polarization to maximize the reflectance efficiency of the SLM. In order to illuminate a larger area of the SLM, a lens system formed by L_3 and L_4 (with focal distances of 50 mm and 100 mm) expands the beam, resulting in a full-width at half maximum (FWHM) diameter of 3.5 mm. A Holoeye PLUTO-VIS phase-only SLM is then employed in reflection mode to direct the beam towards the mirror (M) and the L_5 lens (having a focal distance of 300 mm) that focuses the beam onto a CCD silicon camera.

This setup allows the configuration of different antenna arrays by defining the desired phase mask on the SLM. In our case, the phase mask pattern is generated by multiplying a blazed grating, Fig. 4(b), with a binary matrix representing the elements of the array, Fig. 4(c). The use of a grating as an aperture antenna lets us capture the radiated pattern in the direction of its first diffraction order, thus decreasing the background signal level and noise. At this point, it is important to clarify that the side lobes that appear in the far-field are not result of the different grating orders, but consequence of the array configuration, which is indeed related to its AF. For measurements of SLL, the period of the blazed grating was set to $\Lambda = 102.5\,\mu\mathrm{m}$. The binary matrices representing different array configurations were formed by square apertures with sides of $262.6\,\mu\mathrm{m}$ (415λ), as shown in Fig. 4(c) for a periodic and a spiral arrays of 64 elements. The center-to-center separation between elements in the periodic square array is $367.7\,\mu\mathrm{m}$ (581λ), whereas for Fermat's spiral this number is used as the minimal separation d.

Phase masks and captured far-field radiation patterns of uniformly arranged arrays are shown in Fig. 5(a) and (b), respectively. Sub-figures (i) and (ii) correspond to arrays with 25 and 64 elements, respectively. The lines in Fig. 5(b) represent the direction where the SLL is maximum,
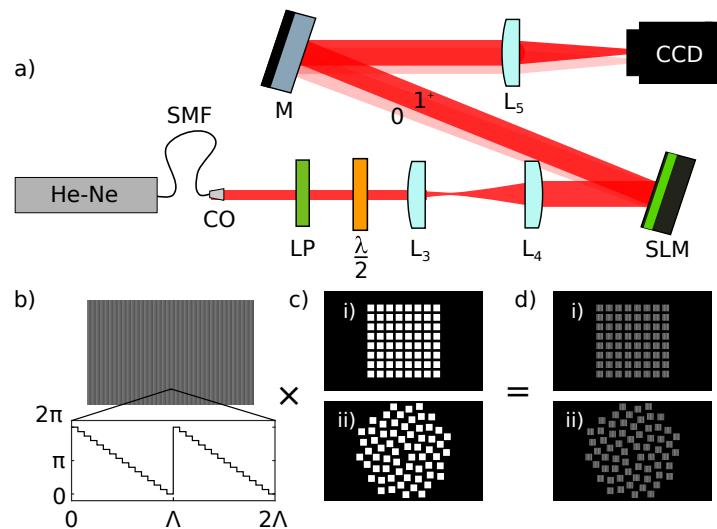
Fig. 4. Sparse array evaluation setup for flexible configurations. (a) Setup for far-field emulation of photonic antennas at 633 nm. SMF: single mode fiber; CO: collimator; LP: linear polarizer; L_3, L_4, and L_5: lenses; SLM: spatial light modulator; M: mirror. 0 and 1^+ indicate the two main diffraction orders. (b) Blazed grating on the SLM. The detailed view shows the phase profile for 2 grating periods, Λ. (c) Element matrices (example with 64-elements) for (i) periodic and (ii) spiral arrangements. (d) Resulting phase masks for the same arrangements.

that is, the worst-case scenarios. Fig. 5(c) shows the normalized intensities along those directions for the three array sizes, as well as the radiation pattern of a single element in the same directions. Similarly, Fig. 5(d), (e), and (f) represent the phase masks, far-fields, and normalized intensities (the latter also in the direction of highest SLL) but for arrays following Fermat's spiral. For comparison, the same number of elements as in the square array are used. The high intensity of the SLL for the periodic array is evident in the far-field images presented in Fig. 5(b). For the aperiodic case, their intensity levels of the secondary lobes are clearly lower than in the periodic configuration.

The SLLs for the different configurations are calculated analogously to the case of the CMOS antennas, that is, extracting the AF by subtracting the normalized radiation pattern of a single element from that of the array. Therefore, from Fig. 5(c), we can see that the SLL of the uniform arrays is, as theoretically predicted, 0 dB for the three array sizes. In contrast, the spiral arrangement of elements results in a radiation pattern with a significantly lower SLL as can be appreciated in Fig. 5(d), revealing a SLL reduction of 5.9 and 6.9 dB for arrays with 25 and 64 elements, respectively. It is also noticeable that for Fermat's spiral, the maximum intensity of the secondary lobe reduces as the number of elements grows. For a target SLL, this poses a lower bound to the number of elements required in the array.

These experiments were repeated for array sizes ranging from 4 to 64 elements. The obtained data are presented in Fig. 6 alongside the SLL of the uniform and spiral arrays fabricated in silicon. As expected from the theoretical analysis (represented by solid lines), the uniform distribution leads to AFs with secondary lobes as intense as its main lobe regardless of the array size. On the other hand, in the aperiodic arrays, the intensity levels of the secondary lobes are significantly lower than that of the main lobe, i.e., the SLL is reduced. Fig. 6 shows that, as predicted in [32], the more elements that are inserted in the array, the higher the SLL reduction. For instance, in the case of the fabricated array with 8-elements, the SLL of the spiral array is 0.9 dB, whereas for
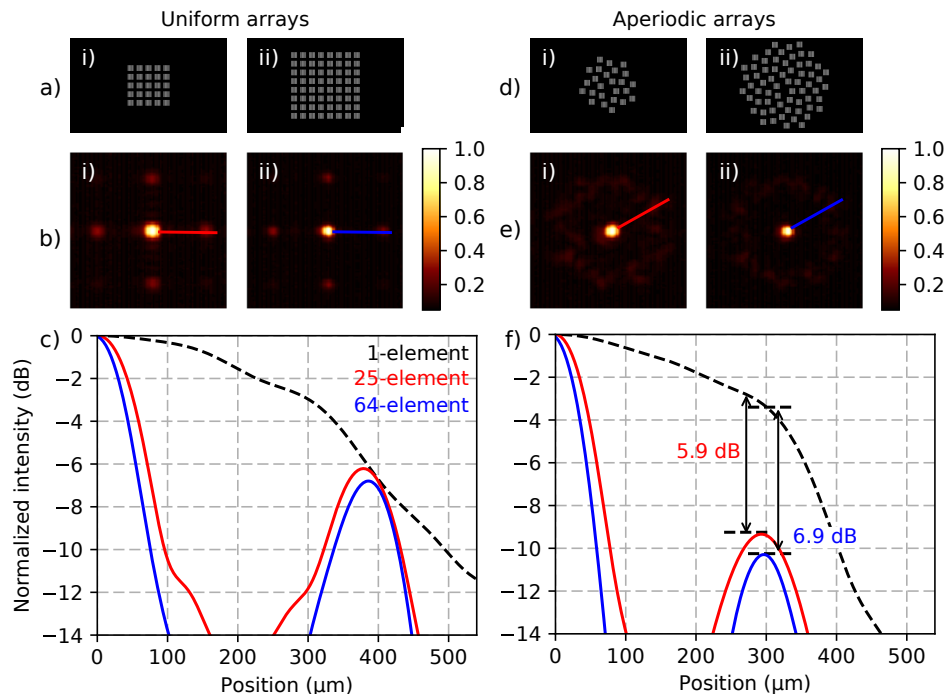
Fig. 5. Far-field radiation patterns for different phased-array configurations. (a) Phase masks and (b) captured far-field radiation patterns for uniform arrays with (i) 25 and (ii) 64 elements. The lines in (b) represent the directions where the secondary lobe is maximum. (c) Normalized far-field intensity along the lines of maximal SLL, represented by the straight lines in (b). For reference, the radiation intensity for a single element is represented in the dashed line. (d-f) Phase-masks, captured far-fields, and normalized far-field intensities in the maximal SLL directions for Fermat's spiral with 25 and 64 elements.

64-elements it rises up to 6.9 dB. The disagreement with the theory observed for the fabricated antennas can be attributed to the limited fabrication resolution and the roughness, while for arrays with sizes above 36, it most probably comes from the combined effects of the limited resolution in antenna positioning in the SLM (spatial discretization of the phase mask) and the limited width of the illumination beam on the SLM, which results in a reduced contribution from the antennas on the periphery of the beam to the total far-field. It is worth noting that an additional advantage of the aperiodic array is the flexibility to allow any number of antennas, not only perfect squares, as is the case for periodic square arrays.

4. Conclusions

In summary, we have demonstrated that the use of Fermat's spiral as an arrangement for the elements of an optical phased array antenna leads to reduction of their SLL. We achieve a SLL reduction of 0.9 dB for a fabricated CMOS-compatible 8-element array antenna. This feature is further confirmed for arrays with higher numbers of elements through an SLM-based emulation, revealing a SLL reduction of up to 6.9 dB for 64-elements. Our results also show that the performance of Fermat's spiral array extends far beyond the usual inter-antenna spacings in sparse arrays, demonstrated for distances of 581λ. The solution presented is thus an attractive array design to prevent multiple radiation lobes with the same radiation level from causing interference, security breaches, and crosstalk in optical wireless systems.
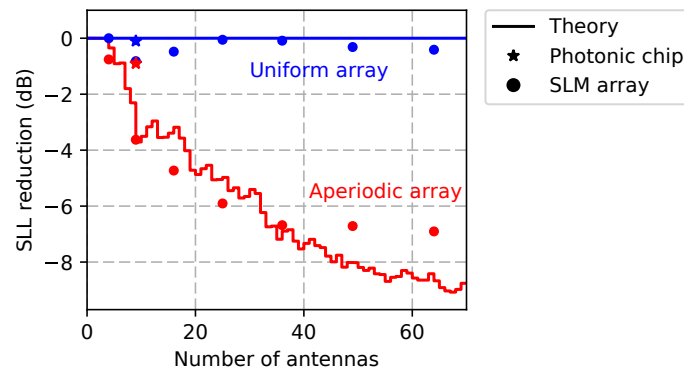
Fig. 6. SLL of both periodic square arrays and Fermat's spiral with different numbers of antennas. As predicted by theory, the SLL remains around 0 dB for the uniform arrays, being independent of the number of elements. In contrast, for the Fermat's spiral array, as the number of antennas increases, the SLL decreases.